



On the attenuating effect of permeability on the low frequency sound of an airfoil



M. Weidenfeld, A. Manela*

Faculty of Aerospace Engineering, Technion - Israel Institute of Technology, Haifa 32000, Israel

ARTICLE INFO

Article history:

Received 4 October 2015

Received in revised form

19 February 2016

Accepted 4 April 2016

Handling Editor: D. Juve

Available online 26 April 2016

ABSTRACT

The effect of structure permeability on the far-field radiation of a thin airfoil is studied. Assuming low-Mach and high-Reynolds number flow, the near- and far-field descriptions are investigated at flapping-flight and unsteady flow conditions. Analysis is carried out using thin-airfoil theory and compact-body-based calculations for the hydrodynamic and acoustic fields, respectively. Airfoil porosity is modeled via Darcy's law, governed by prescribed distribution of surface intrinsic permeability. Discrete vortex model is applied to describe airfoil wake evolution. To assess the impact of penetrability, results are compared to counterpart predictions for the sound of an impermeable airfoil. Considering the finite-chord airfoil as “acoustically transparent”, the leading-order contribution of surface porosity is obtained in terms of an acoustic dipole. It is shown that, at all flow conditions considered, porosity causes attenuation in outcome sound level. This is accompanied by a time-delay in the pressure signal, reflecting the mediating effect of permeability on the interaction of fluid flow with airfoil edge points. To the extent that thin-airfoil theory holds (requiring small normal-to-airfoil flow velocities), the results indicate on a decrease of ~ 10 percent and more in the total energy radiated by a permeable versus an impermeable airfoil. This amounts to a reduction in system sound pressure level of 3 dB and above at pitching flight conditions, where the sound-reducing effect of the seepage dipole pressure becomes dominant. The applicability of Darcy's law to model the effect of material porosity is discussed in light of existing literature.

© 2016 Elsevier Ltd. All rights reserved.

1. Introduction

When an air vehicle passes through unsteady flow conditions, commonly formed as incoming gust or local turbulence, in either fixed-wing or flapping-flight setup, it experiences time variations in the aerodynamic forces acting on it. These variations are inevitably radiated as sound waves, propagating into the far field through flow pressure fluctuations. Airfoil aerodynamic noise contributes significantly to the sound radiation in this case, and to the noise generated by many other aero-machinery structures, including wind turbines and engine fans. With nowadays increasing interest in controlling sound generation for both civil (reduction of airport and wind farm noise pollution) and military (monitoring acoustic signature) applications, it is important to study novel means by which airfoil aerodynamic noise may be efficiently suppressed [1].

* Corresponding author.

E-mail address: amanela@technion.ac.il (A. Manela).

In searching for an optimal method to minimize airfoil noise, owls are known to have the ability to maintain an almost “silent” flight [2,3]. Considering the growing interest in using biomimetics to improve on engineering applications, it therefore seems natural to study the methods by which owls control their flight acoustic radiation. It is now commonly accepted that owls fly silently owing to main three reasons [2]: a leading edge comb of stiff feathers; a fringe of flexible filaments at the feathers trailing edges; and a soft coating at the upper part of the wings. These features suggest that an appropriate combination of airfoil elasticity, structure porosity and material non-homogeneity may result in considerable decrease in flight aerodynamic noise. Focusing on ongoing efforts to analyze the impacts of the above on sound emission, the present work seeks to study the separate effect of airfoil permeability on its far-field sound at unsteady flow conditions.

The theoretical problem of sound radiation by perforated materials was first treated by Ffowcs-Williams [4], who examined the far-field radiation of turbulence interacting with a uniform array of circular orifices over an infinite plane. Both acoustically “opaque” and “transparent” surfaces were considered, yielding leading monopole and dipole radiations, respectively. Following works have focused on various planar geometries with different forms of structure perforations, and included both theoretical [5–10] and experimental [11,12] investigations. Other configurations, such as acoustic liners [13], sandwich panels [14] and circular cylinders [15,16], have also been considered. In common to all theoretical investigations, the total radiation by a perforated surface was calculated based on detailed analysis of the sound emitted by a single cavity interacting with the flow. In cases where an array of pores was considered, the results for the overall radiation were obtained based on a number density parameter, indicating the number of surface pores per unit area. In a single work where non-uniform perforation has been modeled [5], a comparison between uniform and non-uniform pore distributions is made.

In a recent effort to develop novel noise-control methodologies for reducing fluid-structure interaction sound, a sequence of studies have examined surface porosity as means for passive noise control in finite and semi-infinite transparent configurations. To this end, Geyer et al. [17,18] experimented on the effect of porosity on the sound of an airfoil trailing edge interacting with a turbulent boundary layer. Following works examined the impact of surface perforations in other natural [19] and engineering [20,21] applications. Significant pressure level reduction was measured in some of the cases, and the dependence of sound attenuation efficiency on specific details of surface treatment and perforation extent was tested. The above experimental studies were accompanied by numerical and theoretical investigations. Thus, Bae and Moon [22] demonstrated the dampening effect of a porous trailing edge in a flat plate setup using large-eddy simulations. Jaworski and Peake [23] considered the acoustic field of a turbulent eddy interacting with a semi-infinite poroelastic plate using a Wiener-Hopf asymptotic technique. Khorrami et al. [24] suggested porosity to control rotor tip-clearance-induced noise, and Liu et al. [25] examined the impact of perforated coating on the sound of a tandem-cylinder setup.

While the above works are of valuable practical significance, the numerical efforts involved in the course of analysis are rather demanding. It is therefore of interest to suggest a scheme that is significantly less expensive, yet physically meaningful, as an alternative for studying the problem. The present work suggests such an approach, through incorporation of a thin-airfoil-theory calculation for the near-field, and an acoustic-analogy-based scheme for the far-field. The near-field solution is considerably less demanding than the computational-fluid-dynamics calculations applied in Refs. [22,24,25]; the far-field calculation then uses the near-field description as a source term in a linearized acoustic-analogy formulation. In a sense, the suggested approach takes advantage of previous studies [4,7,8,10], without necessitating exact geometrical knowledge on structure perforations. This is realized through application of Darcy’s law [26,27], according to which the microscopic description of body permeability is replaced by an intrinsic functional relation. This enables study of non-homogeneous porous media (where porosity is non-uniformly distributed along the surface), which was previously tackled only in spherical shell and semi-infinite plate geometries [5].

An outline of the paper follows. We consider a two-dimensional model problem of a thin permeable airfoil subject to leading-edge pitching actuation and incoming flow unsteadiness (incident vorticity). Low-Mach and high-Reynolds number flow conditions are assumed, supporting application of a compact-body description for the acoustic problem. The near- and far-field problems are formulated and analyzed in Section 2. The results, quantifying the effect of airfoil porosity on its acoustic signature, are presented in Section 3. Concluding comments are given in Section 4. An assessment of the applicability of Darcy’s law formulation is made in the Appendix.

2. Problem formulation

Schematic of the problem is shown in Fig. 1. Consider a two-dimensional setup of a porous rigid airfoil of chord $2a$. The airfoil is immersed in uniform flow of speed U in the x_1 -direction. At time $t=0$, sinusoidal leading-edge pitching actuation of the form

$$\left(\frac{\partial \xi}{\partial x_1} \right)_{x_1 = -a} = \bar{\varepsilon}_p \sin(\omega_p t) \quad (1)$$

is commenced. Here, $\xi(x_1, t)$ marks airfoil displacement in the x_2 -direction, $\bar{\varepsilon}_p \ll 1$ in accordance with a linearized formulation (hereafter, overbars mark non-dimensional quantities), and ω_p denotes the pitching frequency. Additionally, the airfoil is subject to aerodynamic loading in the form of an incident line vortex of strength Γ , introduced at $t = 0$ at a prescribed

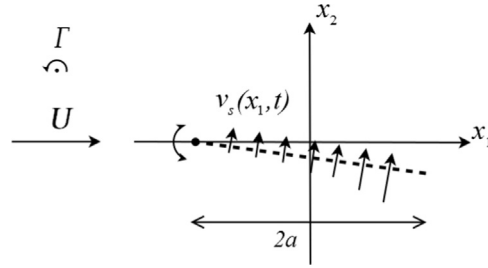


Fig. 1. Schematic of the permeable-airfoil setup.

upstream location. High Reynolds and low Mach number conditions are assumed, so that the near flow field may be considered inviscid and incompressible. Compressibility effects are accounted for when analyzing the far radiated sound.

To model airfoil porosity, Darcy's law formulation is applied [26,27]. Structure penetrability is thus governed by an intrinsic distribution of permeability, a mean representative of material porosity. For clarity of presentation, the distribution is denoted by $\kappa \bar{h}(x_1)$, where κ marks the permeability parameter and $\bar{h}(x_1) \in [0, 1]$ is the corresponding scaled distribution. Vanishing values of \bar{h} represent impermeable points along the chord. In the present thin-airfoil setup, the seepage velocity v_s through the structure is taken proportional to the pressure difference across it [28],

$$v_s(x_1, t) = -\kappa \bar{h}(x_1) \Delta p(x_1, t). \quad (2)$$

In (2), v_s is positive in the x_2 -direction, and $\Delta p(x_1, t) = p_u - p_l$ marks the pressure difference between upper (p_u) and lower (p_l) surfaces of the airfoil. Discussion on the applicability of Darcy's law formulation, traditionally used to analyze small Reynolds number flows through porous media, follows in an Appendix.

In what follows, we investigate the effect of airfoil porosity on airfoil far acoustic signature. To this end, our findings are compared with a reference case of a rigid impermeable airfoil subject to identical excitations. Formulations of the near- and far-field problems are now described.

2.1. Near-field description

The small airfoil deflections prescribed by leading-edge actuation (1), together with high-Reynolds and low-Mach conditions, allow for the application of potential thin airfoil theory approximation to describe the near flow field. Incorporation of the effect of porosity additionally assumes that seepage velocity is generally small compared with the uniform mean speed, $|v_s| \ll U$, which can be *a posteriori* verified. For the present rigid airfoil setup, the leading edge actuation (1) fixes airfoil chord deflection in the x_2 -direction,

$$\xi(x_1, t) = \bar{e}_p(x_1 + a) \sin(\omega_p t), \quad (3)$$

for all $t \geq 0$.

In line with the unsteady flow conditions considered, vortex shedding must occur at the airfoil surface. At the small angles of attack assumed, the flow at the airfoil leading edge is regarded attached, and release of vorticity is allowed only at the surface trailing edge. We make use of a discrete-vortex representation for the airfoil wake, where, at each time step, a concentrated line vortex is released to the flow, with its strength fixed by the Kelvin theorem and the instantaneous time change in airfoil circulation. As indicated by Saffman and Baker [29] and Sarpkaya [30] and references cited therein, discrete models are generally sensitive to the initial locations and core modeling of the nascent vortex. Yet, to the extent that the present small-amplitude setup is considered, our results indicate that the wake description is fully converged in both time and space. At each time step Δt , the nascent point vortex is placed at a distance $U\Delta t$ in the mean-flow direction from the instantaneous position of the trailing edge. Once released, the trajectory of each wake vortex follows from a potential-flow calculation, as formulated below (see Eq. (9)). According to our computations, decrease in the integration time step below some minimum value (see Section 2.3) does not result in any visible changes in system near- and far-field descriptions, thus indicating on scheme convergence.

Using thin-airfoil methodology, the airfoil is represented through its circulation distribution per unit length, $\gamma(x_1, t)$. Using complex notation and denoting the conjugate velocity of the potential flow-field by $W(z)$, the permeability condition is given by

$$\frac{\partial \xi}{\partial t} + U \frac{\partial \xi}{\partial x_1} = -\text{Im}\{W(z)|_{-a \leq x_1 \leq a}\} - v_s, \quad (4)$$

where v_s is specified by Eq. (2), and

$$W(z) = U - \frac{i}{2\pi} \left(\frac{\Gamma}{z - z_r} + \sum_{k=1}^N \frac{\Gamma_k}{z - z_{rk}} + \int_{-a}^a \frac{\gamma(s, t) ds}{z - s} \right). \quad (5)$$

At the airfoil surface

$$W(z)|_{-a \leq x_1 \leq a} = U - \frac{i}{2\pi} \left(\frac{\Gamma}{x_1 - z_I} + \sum_{k=1}^N \frac{\Gamma_k}{x_1 - z_{I_k}} + \oint_{-a}^a \frac{\gamma(s, t) ds}{x_1 - s} \right), \quad (6)$$

where the barred integral sign denotes a Cauchy principal value integral. In (4)–(6), $z = x_1 + ix_2$ marks the complex representation of a point in the plane of motion, and z_I and z_{I_k} denote instantaneous locations of incident and k th trailing edge vortices, respectively. The pressure jump Δp across the airfoil, required for the calculation of seepage velocity v_s , is fixed by the unsteady form of Bernoulli's equation,

$$\Delta p(x_1, t) = \rho_0 U \gamma(x_1, t) + \rho_0 \frac{\partial}{\partial t} \int_{-a}^{x_1} \gamma(s, t) ds, \quad (7)$$

where ρ_0 denotes the fluid mean density.

Incident and wake vortices dynamics are coupled to the system through the right-hand side of the permeability condition (4). The motions of incident and free wake vortices are governed by

$$\frac{dz_I}{dt} = W_I^* \quad (8)$$

and

$$\frac{dz_{I_k}}{dt} = W_{I_k}^* \quad (k = 1, 2, \dots, N), \quad (9)$$

respectively. Here W_I^* and $W_{I_k}^*$ mark the complex conjugates of the conjugate velocities induced at the instantaneous locations of incident and k th free wake vortices, respectively, with their self-singularities removed (cf. (5)),

$$W_I(z) = U - \frac{i}{2\pi} \left(\sum_{k=1}^N \frac{\Gamma_k}{z_I - z_{I_k}} + \int_{-a}^a \frac{\gamma(x_1, t) dx_1}{z_I - x_1} \right) \quad (10)$$

and

$$W_{I_k}(z) = U - \frac{i}{2\pi} \left(\sum_{\substack{m=1 \\ m \neq k}}^N \frac{\Gamma_m}{z_{I_k} - z_{I_m}} + \frac{\Gamma}{z_{I_k} - z_I} + \int_{-a}^a \frac{\gamma(x_1, t) dx_1}{z_{I_k} - x_1} \right). \quad (11)$$

The total system circulation is conserved by applying Kelvin's theorem,

$$\Gamma_N = - \left(\sum_{k=1}^{N-1} \Gamma_k + \int_{-a}^a \gamma(x_1, t) dx_1 \right), \quad (12)$$

which fixes the strength of the nascent vortex Γ_N .

Formulation of the initial-value problem is completed by imposing an initial location for the incident vortex,

$$z_I(t=0) = z_{I_0}, \quad (13)$$

as well as an initial state for the airfoil, prescribed by Eq. (3). To ensure regularization of the flow field at the airfoil trailing edge, the unsteady Kutta condition,

$$\gamma(a, t) = 0, \quad (14)$$

is applied.

The near-field problem formulated above is solved numerically, where shedding of the first trailing vortex occurs at $t=0$. Details regarding the numerical procedure of solution are given in Section 2.3.

2.2. Acoustic-field description

Having formulated the near-field problem, we now turn to analyze the far-field radiation of the system, where the former description serves as an effective “source term”. In the present low-Mach and high-Reynolds number setup, the acoustic field is dominated by a dipole-type interaction between flow vorticity and the solid structure [31]. Surface porosity also affects the far-field in the form of a dipole term, as the airfoil considered is assumed “acoustically transparent” [4].

We start with the equation of vortex sound [31],

$$\left(\frac{1}{c_0^2} \frac{\partial^2}{\partial t^2} - \nabla^2 \right) B = \text{div}(\mathbf{\Omega} \times \mathbf{v}), \quad (15)$$

where c_0 marks the mean speed of sound, $B = \int dp/\rho + v^2/2$ denotes the fluid total enthalpy for homentropic flow (with p, ρ and v marking fluid acoustic pressure, density and velocity magnitude, respectively), \mathbf{v} is the fluid velocity, and $\mathbf{\Omega}$ is the

vorticity vector. The latter is composed of the discrete contributions of incident and wake vortices,

$$\boldsymbol{\Omega} = \boldsymbol{\Omega}_I + \boldsymbol{\Omega}_{I_k}, \quad (16)$$

where

$$\boldsymbol{\Omega}_I = \hat{\mathbf{x}}_3 \Gamma \delta(\mathbf{x} - \mathbf{x}_I(\mathbf{t})) \quad \text{and} \quad \boldsymbol{\Omega}_{I_k} = \hat{\mathbf{x}}_3 \sum_{k=1}^N \Gamma_k \delta(\mathbf{x} - \mathbf{x}_{I_k}(\mathbf{t})), \quad (17)$$

and δ denotes the Dirac delta function. In the far-field ($|\mathbf{x}| \rightarrow \infty$)

$$B(\mathbf{x}, t) \approx p(\mathbf{x}, t)/\rho_0, \quad (18)$$

and we focus on finding the distant $|\mathbf{x}| \rightarrow \infty$ approximation for $p(\mathbf{x}, t)$.

The problem for $B(\mathbf{x}, t)$ is analyzed using a Green's function approach. Towards this end, we introduce a counterpart problem for the Green's function G ,

$$\left(\frac{1}{c_0^2} \frac{\partial^2}{\partial t^2} - \nabla^2 \right) G(\mathbf{x}, \mathbf{y} | t - t_0) = \delta(\mathbf{x} - \mathbf{y}) \delta(t - t_0), \quad (19)$$

where \mathbf{x} and \mathbf{y} denote observer and point-source vector locations, respectively, and t_0 marks the time instant of source action. Taking account of the body surface, and with no loss of generality, we impose a Neumann-type boundary condition of a vanishing normal derivative of G over the airfoil surface, $(\partial G / \partial y_n)_{\text{airfoil}} = 0$. Multiplying Eq. (15) by $G(\mathbf{x}, \mathbf{y} | t - \tau)$, subtracting Eq. (19) multiplied by $B(\mathbf{x}, t)$, and integrating over the volume of fluid and time, we obtain an expression for $B(\mathbf{x}, t)$ in terms of the Green's function,

$$B(\mathbf{x}, t) = - \int_{-\infty}^{\infty} d\tau \int_{-\infty}^{\infty} (\boldsymbol{\Omega} \times \mathbf{v}) \nabla G d^3 \mathbf{y} + \int_{-\infty}^{\infty} d\tau \oint_{\text{airfoil}} \left(B \frac{\partial G}{\partial y_n} + G \frac{\partial v_n}{\partial \tau} \right) dS(\mathbf{y}), \quad (20)$$

where v_n marks the component of fluid velocity normal to the airfoil. Applying the above-mentioned boundary condition for Green's function, and making use of Eq. (18), we arrive at an expression for the far-field acoustic pressure,

$$p(\mathbf{x}, t) \approx - \int_{-\infty}^{\infty} d\tau \int_{-\infty}^{\infty} \rho_0 (\boldsymbol{\Omega} \times \mathbf{v}) \nabla G d^3 \mathbf{y} + \int_{-\infty}^{\infty} d\tau \oint_{\text{airfoil}} \rho_0 G \frac{\partial v_n}{\partial \tau} dS(\mathbf{y}), \quad (21)$$

at $|\mathbf{x}| \rightarrow \infty$.

We consider a case where the airfoil is acoustically compact, in which the characteristic size of the source zone (being the airfoil chord length) is much smaller than the acoustic wavelength. Assuming an acoustic wave with frequency ω_0 and associated wavelength $\lambda_0 = 2\pi c_0 / \omega_0$, this is equivalent to requiring that $a / \lambda_0 = M(\omega_0 a / 2\pi U) \ll 1$, where $M = U / c_0$ is the mean-flow Mach number. At the present low-Mach flow conditions, source compactness is therefore ensured when low to moderate wave frequencies (in convective U/a units) are considered. The appropriate form for the two-dimensional compact Green's function is then [31]

$$G(\mathbf{x}, \mathbf{y}, t - \tau) \approx \frac{\mathbf{x} \cdot \mathbf{Y}}{2\pi \sqrt{2c_0} |\mathbf{x}|^{3/2}} \frac{\partial}{\partial t} \left\{ \frac{H(t_r - \tau)}{\sqrt{t_r - \tau}} \right\}, \quad |\mathbf{x}| \rightarrow \infty, \quad (22)$$

where $t_r \equiv t - |\mathbf{x}| / c_0$ denotes the *acoustic retarded time* and H is the unit step function. $\mathbf{Y}(\mathbf{y})$ marks the *Kirchhoff vector*, which components express flow potentials of unit flow over a thin flat airfoil in the y_1 - and y_2 -directions,

$$\mathbf{Y}(\mathbf{y}) = \left(y_1, \text{Re} \left\{ -i \sqrt{(y_1 + iy_2)^2 - a^2} \right\} \right), \quad (23)$$

respectively.

Making use of the linear property of the far-field problem and the above form of the acoustic Green's function, the acoustic pressure can be expressed as a superposition of “airfoil motion”, “seepage”, “incident vortex” and “wake” contributions,

$$p(\mathbf{x}, t) = p_\xi(\mathbf{x}, t) + p_s(\mathbf{x}, t) + p_I(\mathbf{x}, t) + p_w(\mathbf{x}, t), \quad (24)$$

where

$$p_\xi(\mathbf{x}, t) = \rho_0 \int_{-\infty}^{\infty} \oint_{\text{airfoil}} G(\mathbf{x}, \mathbf{y}, t - \tau) \frac{\partial^2 \xi}{\partial \tau^2} dS(\mathbf{y}) d\tau, \quad (25)$$

$$p_s(\mathbf{x}, t) = \rho_0 \int_{-\infty}^{\infty} \oint_{\text{airfoil}} G(\mathbf{x}, \mathbf{y}, t - \tau) \frac{\partial v_s}{\partial \tau} dS(\mathbf{y}) d\tau, \quad (26)$$

$$p_I(\mathbf{x}, t) = -\rho_0 \int_{-\infty}^{\infty} \int_V (\boldsymbol{\Omega}_I \times \mathbf{V}_I) \cdot \frac{\partial G}{\partial \mathbf{y}}(\mathbf{x}, \mathbf{y}, t - \tau) dS(\mathbf{y}) d\tau, \quad (27)$$

and

$$p_w(\mathbf{x}, t) = -\rho_0 \int_{-\infty}^{\infty} \int_V (\boldsymbol{\Omega}_{\Gamma_k} \times \mathbf{V}_{\Gamma_k}) \cdot \frac{\partial \mathbf{G}}{\partial \mathbf{y}}(\mathbf{x}, \mathbf{y}, t - \tau) d\mathbf{S}(\mathbf{y}) d\tau. \quad (28)$$

In (25)–(28), V denotes the fluid volume occupying all vortices, and \mathbf{V}_{Γ} and \mathbf{V}_{Γ_k} mark the velocity vectors of incident and wake vortices, respectively. Substituting Eqs. (17), (22) and (23) into Eqs. (25)–(28) yields

$$p_{\xi}(\mathbf{x}, t) = \frac{\rho_0 \cos \theta}{2\pi\sqrt{2c_0|\mathbf{x}|}} \frac{\partial}{\partial t} \int_{-\infty}^{t_r} \frac{d\tau}{\sqrt{t_r - \tau}} \int_{-a}^a \sqrt{a^2 - y_1^2} \frac{\partial^2 \xi}{\partial \tau^2}(y_1, \tau) dy_1, \quad (29)$$

$$p_s(\mathbf{x}, t) = \frac{\rho_0 \cos \theta}{2\pi\sqrt{2c_0|\mathbf{x}|}} \frac{\partial}{\partial t} \int_{-\infty}^{t_r} \frac{d\tau}{\sqrt{t_r - \tau}} \int_{-a}^a \sqrt{a^2 - y_1^2} \frac{\partial v_s}{\partial \tau}(y_1, \tau) dy_1, \quad (30)$$

$$p_r(\mathbf{x}, t) = \frac{\rho_0 \Gamma \sin \theta}{2\pi\sqrt{2c_0|\mathbf{x}|}} \frac{\partial}{\partial t} \int_{-\infty}^{t_r} \frac{V_r^{(2)}(\tau) d\tau}{\sqrt{t_r - \tau}} - \frac{\rho_0 \Gamma \cos \theta}{2\pi\sqrt{2c_0|\mathbf{x}|}} \frac{\partial}{\partial t} \int_{-\infty}^{t_r} \frac{d\tau}{\sqrt{t_r - \tau}} \left(V_r^{(1)}(\tau) \frac{\partial Y_2}{\partial y_2} - V_r^{(2)}(\tau) \frac{\partial Y_2}{\partial y_1} \right)_{\mathbf{x}_{\Gamma}(\tau)}, \quad (31)$$

and

$$p_w(\mathbf{x}, t) = \sum_{k=1}^n \left(\frac{\rho_0 \Gamma_k \sin \theta}{2\pi\sqrt{2c_0|\mathbf{x}|}} \frac{\partial}{\partial t} \int_{-\infty}^{t_r} \frac{V_{\Gamma_k}^{(2)}(\tau) d\tau}{\sqrt{t_r - \tau}} - \frac{\rho_0 \Gamma_k \cos \theta}{2\pi\sqrt{2c_0|\mathbf{x}|}} \frac{\partial}{\partial t} \int_{-\infty}^{t_r} \frac{d\tau}{\sqrt{t_r - \tau}} \left(V_{\Gamma_k}^{(1)}(\tau) \frac{\partial Y_2}{\partial y_2} - V_{\Gamma_k}^{(2)}(\tau) \frac{\partial Y_2}{\partial y_1} \right)_{\mathbf{x}_{\Gamma_k}(\tau)} \right). \quad (32)$$

In (31)–(32), $V_r^{(j)}$ and $V_{\Gamma_k}^{(j)}$ mark the incident and k th wake vortex velocity components in the x_j -direction, respectively. The angle θ indicates the far-field observer's directivity, and is measured relative to the x_2 -axis in the clockwise direction. Thus, the $\cos \theta = x_2/|\mathbf{x}|$ and $\sin \theta = x_1/|\mathbf{x}|$ terms in (29)–(32) correspond to “lift” and “suction” dipole-type radiations. Incident and wake vortex sound include both lift and suction dipoles, reflecting vortices velocity components in the y_1 - and the y_2 -direction, respectively. Airfoil motion and seepage velocity radiations, however, contain only a lift component, and thus vanish along the mean-flow ($\theta = \pi/2$) direction.

Calculation of the far-field pressure components is carried out numerically, using the near-field solution in Section 2.1. The only component that can be obtained in a closed form is p_{ξ} , which, by substituting Eq. (3) into (29) and taking a long-time limit, yield

$$p_{\xi}(\mathbf{x}, t) \approx -\frac{\sqrt{\pi}\rho_0 a^3 \cos \theta}{4\sqrt{c_0|\mathbf{x}|}} \bar{\epsilon}_p \omega_p^{5/2} (\cos(\omega_p t_r) + \sin(\omega_p t_r)), \quad t_r \gg \omega_p^{-1}. \quad (33)$$

This indicates on a power increase in airfoil motion sound with increasing pitching frequency ($\sim O(\omega_p^{5/2})$), as reported in Ref. [32].

2.3. Scaling and numerical analysis

To obtain a numerical solution, the dimensional problem formulated in Sections 2.1 and 2.2 is non-dimensionalized using a , U , a/U , $\rho_0 U^2$ and $2\pi a U$ for the length, velocity, time, pressure and vortices circulation, respectively. The non-dimensional form of the penetration condition (4) then becomes

$$\frac{\partial \bar{\xi}}{\partial \bar{t}} + \frac{\partial \bar{\xi}}{\partial \bar{x}_1} = \text{Re} \left\{ \frac{\bar{\Gamma}}{\bar{x}_1 - \bar{z}_r} + \sum_{k=1}^N \frac{\bar{\Gamma}_k}{\bar{x}_1 - \bar{z}_{\Gamma_k}} \right\} + \int_{-1}^1 \frac{\bar{\gamma}(s, \bar{t}) ds}{\bar{x}_1 - s} + 2\pi \bar{\epsilon}_s \bar{h}(\bar{x}_1) \left(\bar{\gamma}(\bar{x}_1, \bar{t}) + \frac{\partial}{\partial \bar{t}} \int_{-1}^{\bar{x}_1} \bar{\gamma}(s, \bar{t}) ds \right), \quad (34)$$

where $\bar{\epsilon}_s = \rho_0 \kappa U \ll 1$ denotes the non-dimensional magnitude of the permeability coefficient. To facilitate formulation, a change of variables $\bar{x}_1 = -\cos \phi$ is introduced, and airfoil circulation distribution $\bar{\gamma}(\phi, \bar{t})$ is expanded in a Fourier sine series

$$\bar{\gamma}(\phi, \bar{t}) = A_0(\bar{t}) \frac{1 + \cos \phi}{\sin \phi} + \sum_{l=1}^L A_l(\bar{t}) \sin l\phi, \quad (35)$$

which identically satisfies the Kutta condition (14). Calculation of the time-dependent Fourier-series coefficients A_l ($l = 1, \dots, L$) is accomplished by grid discretization of the airfoil chord at L grid points, and imposition of the penetration condition at each point. Scheme convergence is validated through a gradual increase in the number of series terms, to an extent where further increase in L has a vanishing effect on the results ($\lesssim 0.1$ percent), typically at $L = 100$.

Following the above-introduced scaling, the non-dimensional parameters governing the dynamical problem are

$$\bar{\epsilon}_s, \quad \bar{\epsilon}_p, \quad \bar{\omega}_p = \frac{\omega_p a}{U}, \quad \bar{\Gamma} \quad \text{and} \quad \bar{z}_{\Gamma_0} = \frac{z_{\Gamma_0}}{a}, \quad (36)$$

specifying the scaled permeability and pitching amplitudes, pitching frequency, and incident vortex strength and initial location, respectively. The problem is also governed by $\bar{h}(\bar{x}_1)$, the specific form of airfoil permeability distribution, to be fixed below (see Eq. (43)). For a given choice of problem parameters, the near-field problem is integrated in time using a fourth-order Runge-Kutta algorithm. A time-step of $\Delta \bar{t} = \pi/400 \bar{\omega}_p$ was found sufficient for convergence of results for a pitching airfoil in steady flow conditions ($\bar{\Gamma} = 0$). In the case of a stationary airfoil in unsteady flow conditions ($\bar{\Gamma} \neq 0$), $\Delta \bar{t} = \pi/400$ ensured convergence.

Applying the same non-dimensionalization to the acoustic problem, the normalized form of the acoustic pressure becomes

$$\bar{p}(\bar{\mathbf{x}}, \bar{t}) = \sqrt{\frac{M}{8|\bar{\mathbf{x}}|}} \Pi_{\text{tot}}(\bar{t}_r) = \sqrt{\frac{M}{8|\bar{\mathbf{x}}|}} (\Pi_\xi(\bar{t}_r) + \Pi_s(\bar{t}_r) + \Pi_r(\bar{t}_r) + \Pi_w(\bar{t}_r)), \quad (37)$$

where

$$\Pi_\xi(\bar{t}_r) = \frac{2}{\pi} \cos \theta \frac{\partial}{\partial \bar{t}} \int_{-\infty}^{\bar{t}_r} \frac{d\tau}{\sqrt{\bar{t}_r - \tau}} \int_{-1}^1 \sqrt{1 - y_1^2} \frac{\partial^2 \bar{\xi}}{\partial \tau^2}(y_1, \tau) dy_1, \quad (38)$$

$$\Pi_s(\bar{t}_r) = \frac{2}{\pi} \cos \theta \frac{\partial}{\partial \bar{t}} \int_{-\infty}^{\bar{t}_r} \frac{d\tau}{\sqrt{\bar{t}_r - \tau}} \int_{-1}^1 \sqrt{1 - y_1^2} \frac{\partial \bar{v}_s}{\partial \tau}(y_1, \tau) dy_1, \quad (39)$$

$$\Pi_r(\bar{t}_r) = 2\bar{r} \left(\sin \theta \frac{\partial}{\partial \bar{t}} \int_{-\infty}^{\bar{t}_r} \frac{\bar{V}_r^{(2)} d\tau}{\sqrt{\bar{t}_r - \tau}} - \cos \theta \frac{\partial}{\partial \bar{t}} \int_{-\infty}^{\bar{t}_r} \text{Re} \left\{ \frac{(\bar{V}_r^{(1)} + i\bar{V}_r^{(2)}) \bar{z}_r d\tau}{\sqrt{(\bar{t}_r - \tau)(\bar{z}_r^2 - 1)}} \right\} \right), \quad (40)$$

and

$$\Pi_w(\bar{t}_r) = \sum_{k=1}^N 2\bar{r}_k \left(\sin \theta \frac{\partial}{\partial \bar{t}} \int_{-\infty}^{\bar{t}_r} \frac{\bar{V}_{r_k}^{(2)} d\tau}{\sqrt{\bar{t}_r - \tau}} - \cos \theta \frac{\partial}{\partial \bar{t}} \int_{-\infty}^{\bar{t}_r} \text{Re} \left\{ \frac{(\bar{V}_{r_k}^{(1)} + i\bar{V}_{r_k}^{(2)}) \bar{z}_{r_k} d\tau}{\sqrt{(\bar{t}_r - \tau)(\bar{z}_{r_k}^2 - 1)}} \right\} \right). \quad (41)$$

Late-time evaluation of Π_ξ (cf. (33)) yields

$$\Pi_\xi(\bar{t}_r) \approx -\sqrt{\frac{2}{\pi}} \cos \theta \bar{\epsilon}_p \bar{\omega}_p^{5/2} (\cos(\bar{\omega}_p \bar{t}_r) + \sin(\bar{\omega}_p \bar{t}_r)), \quad \bar{t}_r \gg \bar{\omega}_p^{-1}. \quad (42)$$

Results for the acoustic field are presented in terms of the acoustic “kernels” Π_{tot} , Π_ξ , Π_s , Π_r and Π_w . In addition to the above parameters, the acoustic pressure is also governed by the observer far-field directivity, $\theta = \arccos(x_2/|\mathbf{x}|)$.

3. Results

To study the effect of airfoil permeability on its far-field radiation, we focus on a case where

$$\bar{h}(\bar{x}_1) = 0.5 + 0.5 \tanh(4\bar{x}_1). \quad (43)$$

This represents a smoothly varying permeability distribution function, having a vanishing value at the airfoil leading edge, and monotonically increasing to a maximum at its trailing edge (see Figs. 2b and 5b). Our calculations indicate that the

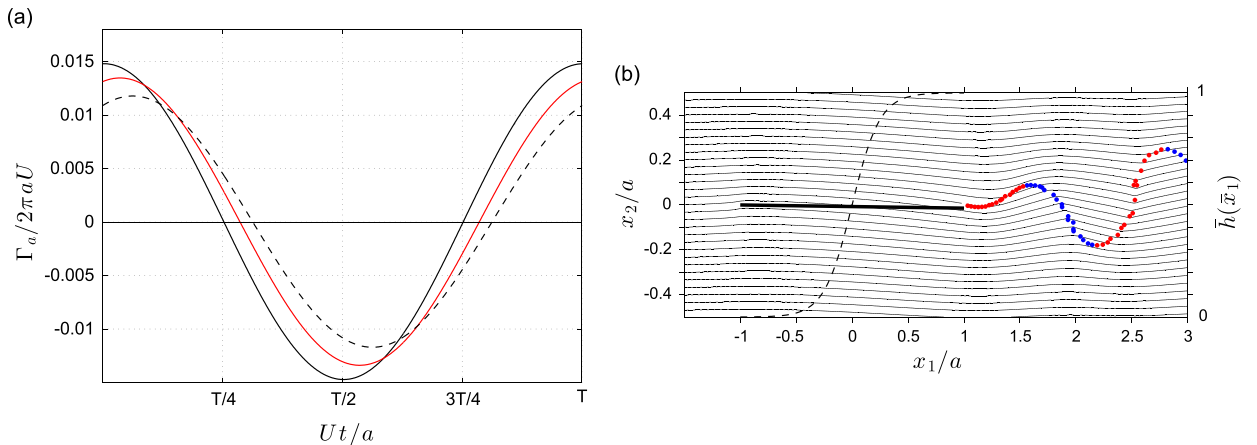


Fig. 2. Near-field characteristics of a permeable airfoil in steady flow ($\bar{T}=0$) pitching at $\bar{\omega}_p=5$. (a) Time-variation of total airfoil circulation for an impermeable airfoil ($\bar{\epsilon}_s=0$, solid line) and permeable airfoils with $\bar{\epsilon}_s=0.05$ (red line) and $\bar{\epsilon}_s=0.1$ (dashed curve). The thin solid horizontal line shows line of zero circulation, for reference. (b) Instantaneous streamline map at time $\bar{t}=0.625T$ for the case $\bar{\epsilon}_s=0.1$. The bold solid line indicates airfoil position, and red and blue dots mark instantaneous locations of wake vortices with positive and negative circulations, respectively. The dashed curve shows airfoil permeability distribution, $\bar{h}(\bar{x}_1)$ (right vertical axis). (For interpretation of the references to color in this figure caption, the reader is referred to the web version of this paper.)

results obtained remain qualitatively similar when varying the distribution function to other monotonically increasing functions, and we therefore skip further discussion on this effect.

To present our findings, we consider separate cases of an actuated airfoil in a steady flow, $\bar{T} = 0$ (Section 3.1), and a stationary airfoil in an unsteady flow, $\bar{\epsilon}_p = 0$ (Section 3.2). In both cases, the effect of airfoil permeability is studied through varying the value of permeability amplitude parameter $\bar{\epsilon}_s$. A comparison with a reference case of an impermeable airfoil, $\bar{\epsilon}_s = 0$, is made.

3.1. Actuated airfoil in steady flow

To investigate the near- and far-field impact of airfoil permeability in steady pitching flight, we fix the pitching amplitude at $\bar{\epsilon}_p = 0.01$ and inspect the effect of varying the pitching frequency $\bar{\omega}_p$ and permeability parameter $\bar{\epsilon}_s$ on the results. For the initial-value problem considered, the system exhibits initial transient behavior in response to the leading-edge actuation (1). In what follows we focus only on the “late-time” periodic response of the system, achieved at $\bar{t} \gg \bar{\omega}_p^{-1}$, practically after only few pitching periods. Following results are presented over a time interval of a pitching period, $0 \leq \bar{t} \leq T$, where $T = 2\pi/\bar{\omega}_p$.

Fig. 2 examines the effect of permeability on the near-field characteristics of an airfoil in steady flow actuated at $\bar{\omega}_p = 5$. In Fig. 2a, the effect of permeability on total airfoil circulation,

$$\bar{\Gamma}_a(\bar{t}) = \int_{-1}^1 \bar{\gamma}(s, \bar{t}) \, ds,$$

is shown. In Fig. 2b, instantaneous streamline and vortical map of a permeable airfoil is presented. For reference, the dashed line in Fig. 2b shows airfoil permeability profile, $\bar{h}(\bar{x}_1)$, as specified in Eq. (43).

Structure permeability is known to reduce the aerodynamic efficiency of an airfoil, as demonstrated by Iosilevskii [28]. It is therefore expected that higher permeability values are accompanied by lower airfoil circulations, which correspond to decreasing lift forces. Such is the result shown in Fig. 2a, where decreasing amplitudes in $\bar{\Gamma}_a$ are obtained for an actuated airfoil with increasing permeability coefficient. The results also indicate on a phase-shift in circulation maxima and minima times caused by airfoil permeability. Since release of trailing edge vorticity is directly affected by changes in airfoil circulation, counterpart phase lag between release of positive and negative trailing vorticity is also viewed between airfoils with different permeability coefficients. This reflects on the predictions of airfoil wake noise, to be presented in Fig. 3.

The streamline and vortical map presented in Fig. 2b shows a time snapshot of the near-field flow at time $\bar{t} = 0.625 T$, when the airfoil is displaced half-way below its unperturbed state (see Eq. (3)). At this time instant, flow streamlines are seen to penetrate the airfoil, partially owing to its actuation-induced velocity, but also due to its permeability. The oscillatory trailing edge wake is composed of vortices having positive and negative circulations, balancing, at each time instant, the transitory value of airfoil circulation and sum of circulations of all previously released vortices (see Eq. (12)). A similar qualitative result was obtained in the case of an impermeable airfoil, and is skipped here for brevity.

Traversing to the far-field radiation of the system, Fig. 3 describes the acoustic signature of permeable and impermeable airfoils at the same $\bar{\omega}_p = 5$ conditions considered in Fig. 2. Results focus on the lift ($\theta = 0$) dipole contribution, and display data in terms of the radiation kernels (37)–(41). Typically, the suction dipole is one order of magnitude (or more) smaller than the lift component, and is therefore not discussed in separate.

Starting with Fig. 3a, the motion sound component (Π_ξ , solid line) is common to all cases, permeable or not. The seepage dipole then adds only to the permeable airfoil radiation, and increases in amplitude with increasing $\bar{\epsilon}_s$. Notably, the seepage component acts in a nearly opposite phase to the motion dipole, tending to reduce direct motion sound. This can be physically rationalized, as our calculations indicate that while a permeable section of the airfoil translates in the positive x_2 -direction, it induces a seepage velocity in the negative x_2 -direction, and thus reduces the total normal-to-surface fluid velocity at the surface, together with its accompanying acoustic signal. A similar sound-reducing effect of permeability is observed in Fig. 3b, where the wake dipole contribution Π_w is compared between impermeable and permeable airfoils. According to Kelvin’s theorem (Eq. (12)), the total wake circulation amounts to the total airfoil circulation (in a negative sign). The reduction in wake sound amplitude is therefore attributed to the smaller rate of trailing-edge vorticity generated at larger values of $\bar{\epsilon}_s$, as supported by the results in Fig. 2a. Also supported by Fig. 2a is the phase shift in acoustic wave maxima and minima, obtained between different values of $\bar{\epsilon}_s$. The total sound radiation, presented in Fig. 3c, shows the total sum of motion, seepage and wake noise components, and demonstrates the general attenuating effect of airfoil permeability on the radiated sound amplitude in the x_2 -direction. In terms of sound pressure level, the difference in the maximum value of Π_{tot} between impermeable and permeable airfoil with $\bar{\epsilon}_s = 0.1$ amounts to a 3.1 dB reduction in the permeable case.

To account for sound radiation in all directions, Fig. 3d presents the effect of airfoil permeability on the system acoustic power,

$$\mathcal{P}_{\text{acous}}(\bar{t}_r) = \int_0^{2\pi} \Pi_{\text{tot}}^2(\bar{t}_r, \theta) \, d\theta, \quad (44)$$

defined, in a non-dimensional form, by an integral on the square of the total radiation (37) over a large-radius ($|\bar{\mathbf{x}}| \rightarrow \infty$) circle. Having incorporated the effects of lift and suction dipoles into $\mathcal{P}_{\text{acous}}$, the results in Fig. 3d reiterate on the sound-dampening effect of airfoil permeability, in terms of both acoustic pressure maxima and total radiation, as reflected by the decrease in area below the curves with increasing $\bar{\epsilon}_s$.

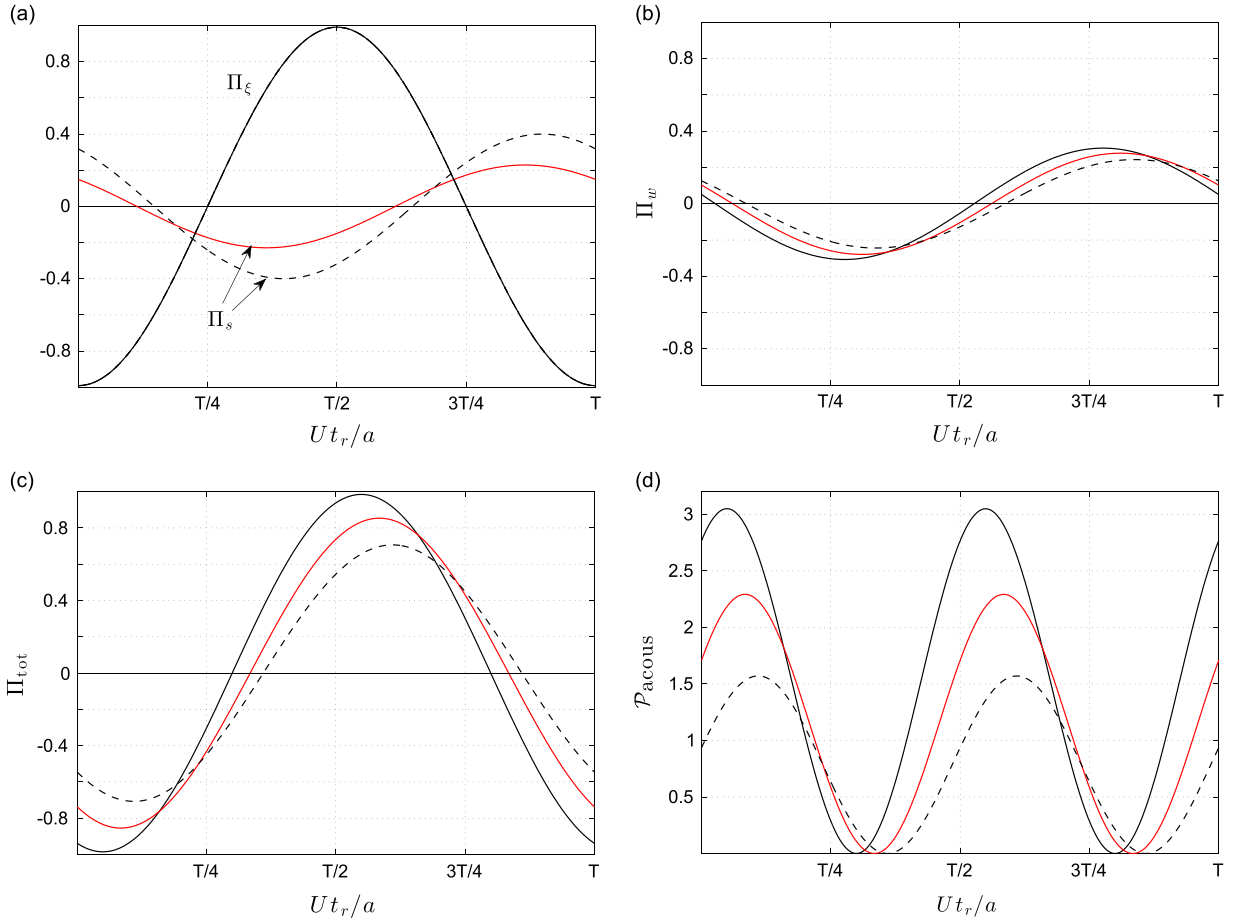


Fig. 3. Far-field radiation of a permeable airfoil in steady flow ($T = 0$) pitching at $\bar{\omega}_p = 5$. (a) Direct motion noise Π_ξ (solid line) and seepage sound Π_s in the normal x_2 -direction at $\bar{\varepsilon}_s = 0.05$ (red curve) and $\bar{\varepsilon}_s = 0.1$ (dashed line). (b and c) Wake sound (b) and total radiation (c) in the x_2 -direction for airfoils with $\bar{\varepsilon}_s = 0$ (solid lines, impermeable airfoil), 0.05 (red lines), and 0.1 (dashed curves). (d) System acoustic power for airfoils with $\bar{\varepsilon}_s = 0$ (solid line, impermeable airfoil), 0.05 (red line), and 0.1 (dashed curve). Thin horizontal lines in (a–c) mark lines of zero pressure, for reference. (For interpretation of the references to color in this figure caption, the reader is referred to the web version of this paper.)

The effect of pitching frequency on the system far-field radiation is now discussed. Towards this end, we introduce the system *total sound energy*,

$$\mathcal{P}_{acous}^* = \int_{\bar{t}_i}^{\bar{t}_f} \mathcal{P}_{acous}(\tau) d\tau, \quad (45)$$

measuring the total sound radiated by the system during a time interval $\bar{t}_r \in [\bar{t}_i, \bar{t}_f]$. Fig. 4 presents the variation with pitching frequency $\bar{\omega}_p$ of the ratio between total sound energy of permeable and impermeable airfoils, $\mathcal{P}_{acous}^* / \mathcal{P}_{acous}^{*, \bar{\varepsilon}_s = 0}$, during a fixed time interval, $\bar{t}_r \in [11, 20]$. The time interval of integration is chosen equal for all frequencies, to enable comparison between results at different values of $\bar{\omega}_p$. From the observer point of view, it appears reasonable to consider a fixed time-frame as a basis for comparison, as the difference in pitching conditions should not affect the time duration of external observation.

Common to all curves in Fig. 4 is a monotonic decrease in $\mathcal{P}_{acous}^* / \mathcal{P}_{acous}^{*, \bar{\varepsilon}_s = 0}$ with increasing frequency. This reflects on an increase in the sound-attenuating effect of permeability, at fixed $\bar{\varepsilon}_s$, with increasing $\bar{\omega}_p$. Thus, even for a relatively low $\bar{\varepsilon}_s = 0.025$ value of the permeability coefficient, the total sound energy of a reference impermeable airfoil is reduced by more than 10 percent at $\bar{\omega}_p = 5$. The effect becomes more pronounced with growing $\bar{\varepsilon}_s$. At the highest $\bar{\varepsilon}_s = 0.1$ value examined, the relative reduction in sound energy exceeds 45 percent for $\bar{\omega}_p = 5$. In view of the $\bar{\omega}_p^{5/2}$ increase in airfoil motion noise component in the case of an impermeable airfoil (see Eq. (42)), this sound-reduction mechanism may prove of practical importance.

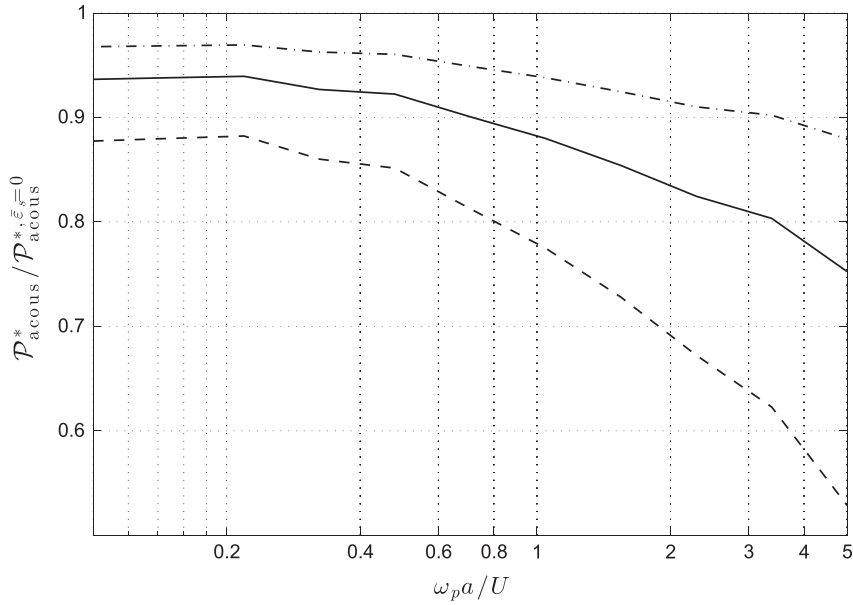


Fig. 4. Effect of pitching frequency $\bar{\omega}_p$ on the ratio between system total sound energy $\mathcal{P}_{\text{acous}}^*$ for permeable and impermeable airfoils. Dash-dotted, solid and dashed lines mark results for airfoils with $\bar{\varepsilon}_s = 0.025, 0.05$ and 0.1 , respectively. In all cases, the total sound energy is calculated over a time interval of $\bar{t}_r \in [11, 20]$ (see Eq. (45)).

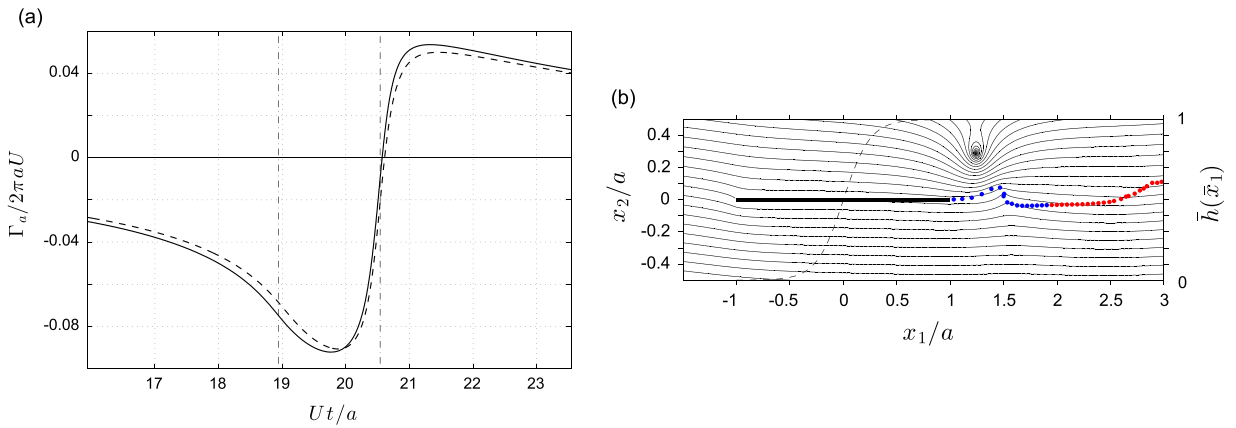


Fig. 5. Near-field characteristics of a stationary ($\bar{\varepsilon}_p = 0$) airfoil in unsteady ($\bar{\Gamma} = 0.2$) flow. (a) Time-variation of total airfoil circulation during vortex passage above airfoil. Solid and dashed lines mark airfoils with $\bar{\varepsilon}_s = 0$ (impermeable) and $\bar{\varepsilon}_s = 0.1$, respectively. Vertical dash-dotted lines confine the time interval during which the vortex passes above the airfoil. Thin horizontal line marks line of zero circulation, for reference. (b) Instantaneous streamline map at time $\bar{t} = 20.8$ for the case $\bar{\varepsilon}_s = 0.1$. Bold solid line indicates airfoil position, and red and blue dots mark locations of wake vortices with positive and negative circulations, respectively. The dashed curve shows airfoil permeability distribution, $\bar{h}(\bar{x}_1)$ (right vertical axis). (For interpretation of the references to color in this figure caption, the reader is referred to the web version of this paper.)

3.2. Stationary airfoil in unsteady flow

Considering the effect of airfoil permeability on the near- and far-field properties of a non-actuated structure, we fix the incident vortex strength to $\bar{\Gamma} = 0.2$ and set $\bar{\varepsilon}_p = 0$ (see Eq. (36)). Formulation of the initial-value problem is obtained by prescribing the initial location of the incident vortex, $\bar{z}_{r0} = -20 + 0.2i$, sufficiently upstream of the airfoil to capture the entire process of vortex–airfoil interaction. Following results investigate on the impact of $\bar{\varepsilon}_s$ on the interaction of incoming flow unsteadiness with the structure.

Fig. 5 describes the effects of airfoil permeability on its near-field characteristics in the vortex-excited case. In parallel with Fig. 2, Fig. 5a presents time-variation of total airfoil circulation during vortex passage above the structure, and Fig. 5b shows instantaneous streamline and vortical map of the system at time $\bar{t} = 20.8$. To clarify presentation, the time interval during which the incident vortex passes above the airfoil is delineated by vertical dash-dotted lines in Fig. 5a. This time interval varies only slightly between the different values of $\bar{\varepsilon}_s$ considered.

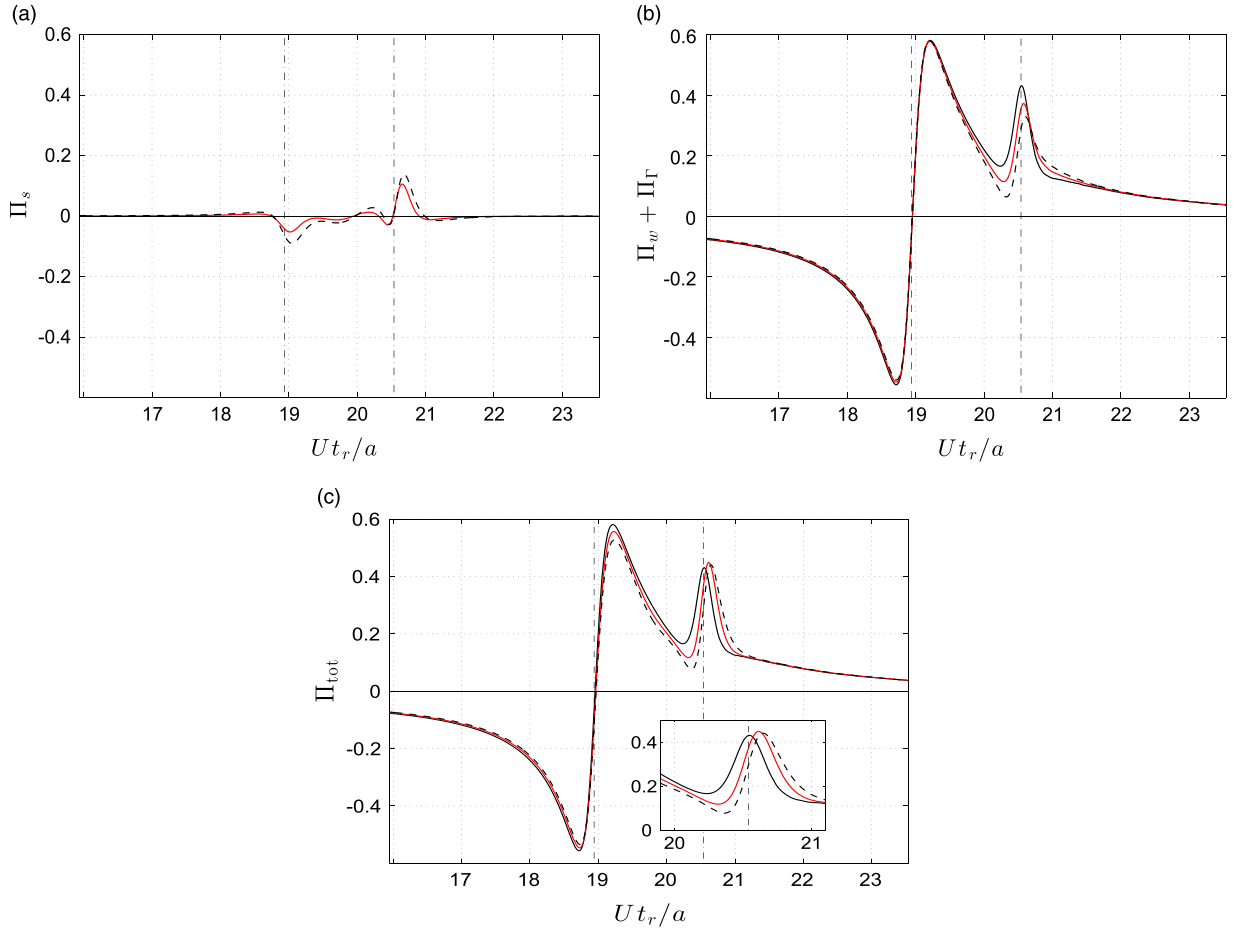


Fig. 6. Far-field radiation in the normal x_2 -direction for a stationary ($\bar{\varepsilon}_p = 0$) airfoil in unsteady flow ($\bar{\Gamma} = 0.2$). (a) Seepage noise component Π_s . (b) Sum of wake and incident vortex contributions, $\Pi_w + \Pi_\Gamma$. (c) Total radiation, Π_{tot} . In all parts, solid, red and dashed curves mark data for airfoils with $\bar{\varepsilon}_s = 0, 0.05$ and 0.1 , respectively. Vertical dash-dotted lines confine the time interval during which the vortex passes above the airfoil. Thin horizontal lines mark lines of zero pressure, for reference. The inset in (c) shows a zoom into the total signature in the proximity of trailing edge time.

In Fig. 5a, the effect of structure permeability on airfoil circulation appears minor, yet consistent in that the overall $\bar{\Gamma}_a$ -variation is smaller in the permeable case, and is shifted to slightly later times (cf. Fig. 2a). In the streamline map of Fig. 5b, structure permeability is reflected via the streamlines penetrating the airfoil at its lower surface close to the trailing edge. At the time instant $\bar{t} = 20.8$ presented, the incident vortex is located at $(\bar{x}_1, \bar{x}_2) \approx (1.2, 0.25)$, distorting the streamlines in its vicinity according to its induced velocity. The shedding of vorticity consists of trailing vortices with negative circulation (marked in blue). This is in line with the Kelvin theorem (12) and the instantaneous variation in airfoil circulation, which is monotonically increasing (see Fig. 5a). Notably, the passage of incident vortex above the airfoil edge distorts the location of trailing vortices, by applying an upward “bent” to the wake form. This is caused by the nonlinear interactions between vortices trajectories, formulated in Section 2.1, and affects the system acoustic far field, as discussed below.

The impact of airfoil permeability on its far-field properties in the unsteady case is described in Fig. 6. Focusing on the lift-dipole component, Figs. 6a and 6b present separate contributions of seepage (Π_s) and wake and incident vortices ($\Pi_w + \Pi_\Gamma$) to the airfoil signature, respectively. Fig. 6c describes the total lift dipole of the system, Π_{tot} . The contribution of direct airfoil motion noise, Π_s , is obviously missing in this case, as the structure is stationary.

Starting with Fig. 6a, we find that Π_s , non-existing in the impermeable case, increases in magnitude with increasing $\bar{\varepsilon}_s$. For a given value of $\bar{\varepsilon}_s$, the seepage noise component becomes maximal (in absolute value) at incident vortex leading- and trailing-edge times, marked by the left- and right-hand vertical dash-dotted lines, respectively. This is since, at these times, the interaction of the vortex with the airfoil is most intense, causing extremal values in the seepage velocity v_s and its time derivatives. Moving to the total vortex sound contribution in Fig. 6b, we observe that the signal is nearly unaffected by airfoil permeability at times prior to trailing-edge time. Yet, a sound-attenuating effect (opposite to the sound magnifying effect in Fig. 6a) of permeability is seen at trailing-edge time, indicating that permeability dampens the aerodynamic loading induced by the incident vortex interaction with airfoil edge.

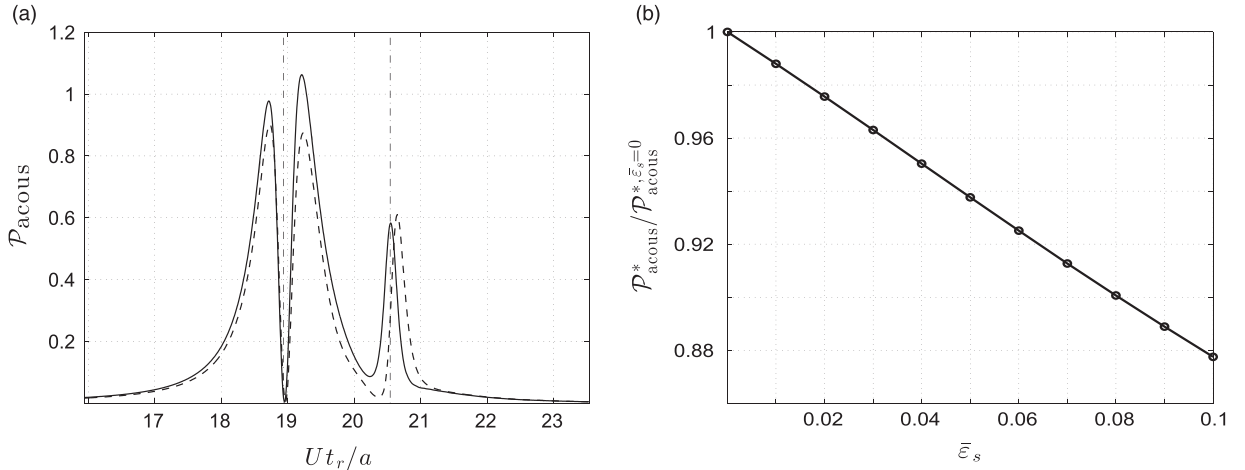


Fig. 7. Far-field radiation for a stationary ($\bar{\epsilon}_p = 0$) airfoil in unsteady ($\bar{T} = 0.2$) flow. (a) Comparison between acoustic power of impermeable ($\bar{\epsilon}_s = 0$, solid line) and permeable ($\bar{\epsilon}_s = 0.1$, dashed curve) airfoils. Vertical dash-dotted lines confine the time interval during which the vortex passes above the airfoil. (b) Effect of permeability parameter $\bar{\epsilon}_s$ on the ratio between system total sound energy P_{acous}^* for permeable and impermeable airfoils. The total sound energy in each case is calculated over a time interval of vortex passage between $\bar{x}_1 = -5$ and $\bar{x}_1 = 5$ (see Eq. (45)).

Summing Figs. 6a and 6b to obtain Fig. 6c it is found that, although the seepage pressure is much smaller in magnitude compared with vortex sound, it has a visible effect on the total radiation. Thus, at leading-edge time, seepage sound acts to reduce vortex sound, causing a slight attenuation in the maximum pressure level right to the first dash-dotted line. At trailing-edge time (zoomed in the inset in Fig. 6c), the attenuating effect of permeability is caused mainly by the reduction in vortex sound observed in Fig. 6b. A time phase-shift effect of $\bar{\epsilon}_s$, reminiscent of the time-shift found for an actuated airfoil in Fig. 3, is also visible in the total signal.

To conclude the discussion on the effect of permeability in the unsteady case, Fig. 7 presents results for the acoustic power and total sound energy of the system. Fig. 7a compares between the acoustic power of impermeable and permeable airfoils. Fig. 7b describes the impact of $\bar{\epsilon}_s$ on the ratio between the total sound energy P_{acous}^* for permeable and impermeable airfoils. For the calculation of P_{acous}^* , the time interval taken was the time during which the incident vortex passes between $\bar{x}_1 = -5$ and $\bar{x}_1 = 5$ (see Eq. (45)), so that the core effect of near vortex–airfoil interaction is taken into account.

In line with the results in Fig. 6, the data in Fig. 7a reconfirms that permeability dampens sound levels at all times, particularly during leading- and trailing-edge interactions. The continuous effect of increasing $\bar{\epsilon}_s$ is presented in Fig. 7b, where a monotonic (nearly linear) decrease in P_{acous}^* is found. Specifically, the decrease amounts to slightly more than 12 percent for $\bar{\epsilon}_s = 0.1$. This result, combined with the findings in Fig. 4 for an actuated airfoil, quantitates the overall impact of permeability on the far-field pressure level of the system, according to the present model.

4. Conclusion

We studied the effect of structure permeability on the far-field radiation of a thin airfoil. Considering low-Mach and high-Reynolds number flow, the near- and far-field descriptions were investigated at flapping-flight and unsteady flow conditions. Analysis was carried out based on thin-airfoil theory and compact-body calculations for the hydrodynamic and acoustic fields, respectively. Airfoil porosity was modeled using Darcy's law, governed by a prescribed distribution of surface intrinsic permeability. Considering the finite-chord airfoil as “acoustically transparent”, the leading-order contribution of surface porosity was obtained in terms of an acoustic dipole, and the total acoustic signature was compared with that of an impermeable airfoil. It was shown that, at all flow conditions considered, porosity attenuates the outcome sound level. This is accompanied by a time-delay in the pressure signal, reflecting the mediating effect of permeability on the interaction of fluid flow with airfoil edge points. The results indicate on a decrease of ~ 10 percent and more in the total energy radiated by a permeable versus an impermeable airfoil. This amounts to a reduction in system sound pressure level of 3 dB and above when considering pitching flight conditions, where the sound-reducing effect of the seepage dipole p_s becomes dominant.

Perhaps the main approximation made through the analysis, apart from relying on thin-airfoil theory and considering compact-body conditions, was in applying Darcy's law to model structure permeability. This assumes that the Reynolds number based on surface permeability and pore flow velocity does not exceed unity, and that the characteristic time-scale of porous effects is shorter than the aerodynamic scale. It is verified in the Appendix that such conditions may be feasibly assumed. Having based our calculations on Darcy's model, the scheme of solution does not necessitate exact geometrical knowledge on structure perforations, and only requires an average macroscopic description in terms of intrinsic porosity distribution. This may be considered advantageous over previous studies on porous-body radiation [4,7,8,10], where such detailed information has limited analysis to only homogeneous pore arrays. While a single example of a non-homogeneous

distribution was considered here (see Eq. (43)), our scheme can be readily applied to study any other distribution that agrees with model assumptions.

A desirable verification of our results may be obtained by means of computational aeroacoustics (CAA) calculations. Within the context of complex fluid–structure interactions with perforated materials, such investigations are considerably resource-demanding and difficult to carry out. This is perhaps the reason for the small number of numerical analyses appearing in literature on this topic [22,33], among which only Ref. [22] applies the macroscopic Darcy's and Ergun's formulations. In this respect, the purpose of the present work is to apply a similar macroscopic approach to evaluate the far-field sound of a permeable airfoil via a compact Green's function formulation. The challenging task of numerical validation of our results by means of CAA calculations is not in the scope of the present contribution, and is considered it as a topic for future study.

Recalling the challenge in studying the silent flight of owls [2], it is of interest to consider the combined effects of airfoil porosity and elasticity on flight aerodynamic sound. While the separate effect of elasticity has been previously considered (e.g., [32]), a study on the near- and far-fields of a poroelastic airfoil possesses a particular challenge when seeking for optimal conditions to reduce airfoil sound. This is since, even in the simplified thin-airfoil description, the near-field problem is nonlinear, indicating that the total impact of porosity and elasticity cannot be predicted by a simple superposition of the two. A study on the combined noise-control problem is currently in progress.

Appendix A. Applicability of Darcy's law

The Appendix considers the limits of validity of Darcy's law formulation introduced in Eq. (2) for the present problem. The limitations follow from both length- and time-scale considerations, and correspond to steady (uniform incoming flow over a pitching airfoil) and unsteady (non-uniform flow over a stationary airfoil) formulations of the problem.

In its familiar notation, Darcy's constitutive law takes the form [26,27]

$$v_s = -\frac{k}{\mu}\nabla p, \quad (\text{A.1})$$

assuming a linear relation between fluid seepage velocity and pressure gradient, with a constant of proportionality of $1/r = k/\mu$. Here k and μ mark Darcy's conductivity coefficient and fluid dynamic viscosity, respectively, and $r = \mu/k$ denotes the porous media resistivity [17]¹. In general, Darcy's law is valid when the characteristic length- and time-scales of the problem are large compared with their counterpart pore-level scales, $k^{1/2}$ and k/ν , respectively, with ν denoting fluid kinematic viscosity. Additionally, for the formulation to be effective, the Reynolds number based on pores permeability and seepage velocity, $Re_s = v_s k^{1/2}/\nu$, should be sufficiently small ($Re_s \lesssim O(1)$), reflecting the dominance of viscous effects within the pores. At higher values of Re_s , Darcy's model becomes invalid, and should be replaced by a higher-order (quadratic in v_s) law, as suggested by Ergun and others [22,35,36]. Consideration of such a model, however, is not in the scope of the present work.

Starting with the limitation on Re_s , it is required that $v_s k^{1/2} \lesssim 10^{-5}$ m²/s in air. For seepage velocities of order $v_s \approx 1$ m/s (corresponding to an order-of-magnitude higher flight velocities U , to maintain $v_s/U \ll 1$), this corresponds to $k^{1/2} \lesssim 10^{-5}$ m. Referring to Table 1 in Ref. [17], this condition is equivalent to restricting $r \gtrsim 10^5$ kg/m³ s, and is satisfied by various types of synthetic foam materials.

For the infinitely thin porous structure treated in the present work, Darcy's law takes the form of Eq. (2),

$$v_s(x_1, t) = -\kappa \bar{h}(x_1) \Delta p(x_1, t), \quad (\text{A.2})$$

where the pressure gradient in (A.1) is replaced by the pressure jump across the airfoil, and $\kappa = 1/rd$ relates the porous media resistivity r with airfoil thickness d . The associated pore-level time-scale, $t_s = k/\nu = \rho_0 \kappa d$, is now compared with the aerodynamic time-scale, t_a , to specify the required conditions for $t_s \ll t_a$.

Making use of the non-dimensional notation $\bar{v}_s = \rho_0 \kappa U$ (see (34) *et seq.*), t_s is given by $t_s = \bar{v}_s d/U$. In a typical estimation for most birds [37], $d/U \approx 10^{-4}$ s, and the pore-level time-scale estimation becomes $t_s \approx 10^{-5}$ s for the largest value of $\bar{v}_s = 0.1$ considered. Traversing to the aerodynamic time-scale, it may vary between $t_a = a/U$ and $t_a = 1/\omega_p$ for the stationary and non-stationary airfoil problems considered, respectively. These two time-scales are approximately the same, as only $\omega_p a/U \sim O(1)$ values are considered in the flapping-airfoil case. Typically, $t_a = a/U \approx 10^{-2}$ s for most birds [37], and thus the condition $t_s/t_a = \bar{v}_s d/a \ll 1$ is met. In terms of porous media resistivity, the $t_s \approx 10^{-5}$ s estimation corresponds to $r \approx 10^5$ kg/m³ s, in agreement with the value required to satisfy the low Reynolds number condition above.

¹ Previous studies (e.g., [34]) have established relations between the microscopic (detailed pores geometry) and macroscopic Darcy's description in several geometries, yielding formulae for the overall material resistivity in terms of pores configuration.

References

- [1] O. Zaporozhets, V. Tokarev, K. Attenborough, *Aircraft Noise*, Taylor and Francis, New York, 2011.
- [2] R.R. Graham, The silent flight of owls, *Journal of the Royal Aeronautical Society* 286 (1934) 837–843.
- [3] E. Sarradj, C. Fritzsche, T. Geyer, Silent owl flight: bird flyover noise measurements, *AIAA Journal* 49 (2011) 769–779.
- [4] J.E. Ffowcs Williams, The acoustics of turbulence near sound-absorbent liners, *Journal of Fluid Mechanics* 51 (1972) 737–749.
- [5] M.S. Howe, On the added mass of a perforated shell, with application to the generation of aerodynamic sound by a perforated trailing edge, *Proceedings of the Royal Society of London A* 365 (1979) 209–233.
- [6] M.S. Howe, The influence of vortex shedding on the diffraction of sound by a perforated screen, *Journal of Fluid Mechanics* 97 (1980) 641–653.
- [7] P.A. Nelson, Noise generated by flow over perforated surfaces, *Journal of Sound and Vibration* 83 (1982) 11–26.
- [8] M.S. Howe, Sound produced by turbulent flow over a perforated inlet, *Journal of Sound and Vibration* 139 (1990) 227–240.
- [9] M.S. Howe, The damping of flexural and acoustic waves by a bias-flow perforated elastic plate, *European Journal of Applied Mathematics* 6 (1995) 307–328.
- [10] M.S. Howe, Sound generated by turbulence and discrete vortices interacting with a perforated elastic plate in low-Mach-number flow, *Quarterly Journal of Mechanics and Applied Mathematics* 50 (1997) 279–301.
- [11] N.S. Dickey, A. Selamet, M.S. Ciray, An experimental study of the impedance of perforated plates with grazing flow, *Journal of the Acoustical Society of America* 110 (2001) 2360–2370.
- [12] S.H. Lee, J.G. Ih, K.S. Peat, A model of acoustic impedance of perforated plates with bias flow considering the interaction effect, *Journal of Sound and Vibration* 303 (2007) 741–752.
- [13] A.B. Bauer, R.L. Chapkis, Noise generated by boundary-layer interaction with perforated acoustic liners, *Journal of Aircraft* 14 (1977) 157–160.
- [14] I.D. Abrahams, Sound radiation from a line forced perforated elastic sandwich panel, *Journal of the Acoustical Society of America* 105 (1999) 3009–3020.
- [15] T. Takaishi, M. Ikeda, C. Kato, Effects of periodic holes on the suppression of aeroacoustic noise from a pantograph horn, *ASME/JSM 2003 4th Joint Fluids Summer Engineering Conference*, Vol. 1, 2003, pp. 41–48.
- [16] I. Yahathugoda, S. Akishita, Investigation on the effect of surface impedance for reducing aerodynamic sound from circular cylinder, *JSM International Journal B* 47 (2004) 67–74.
- [17] T. Geyer, E. Sarradj, C. Fritzsche, Measurement on the noise generation at the trailing edge of porous airfoils, *Experiments in Fluids* 48 (2010) 291–308.
- [18] T. Geyer, E. Sarradj, C. Fritzsche, Porous airfoils: noise reduction and boundary layer effects, *International Journal of Aeroacoustics* 9 (2010) 787–820.
- [19] K. Chen, Q. Liu, G. Liao, Y. Yang, L. Ren, H. Yang, X. Chen, The sound suppression characteristics of wing feather of owl (*bubo bubo*), *Journal of Bionic Engineering* 9 (2012) 192–199.
- [20] H. Hamakawa, K. Hosokai, T. Adachi, E. Kurihara, Aerodynamic sound radiated from two-dimensional airfoil with local porous material, *Open Journal of Fluid Dynamics* 3 (2013) 55–60.
- [21] C. Wang, L. Huang, Passive noise reduction for a contrarotating fan, *ASME Journal of Turbomachinery* 137 (2015) 031007.
- [22] Y. Bae, Y.J. Moon, Effect of passive porous surface on the trailing-edge noise, *Physics of Fluids* 23 (2011) 126101.
- [23] J.W. Jaworski, N. Peake, Aerodynamic noise from a poroelastic edge with implications for the silent flight of owls, *Journal of Fluid Mechanics* 723 (2013) 456–479.
- [24] M. Khorrami, L. Fei, M. Choudhari, Novel approach for reducing rotor tip-clearance-induced noise in turbofan engines, *AIAA Journal* 40 (2002) 1518–1528.
- [25] H.R. Liu, M. Azarpeyvand, J.J. Wei, Z.G. Qu, Tandem cylinder aerodynamic sound control using porous coating, *Journal of Sound and Vibration* 334 (2015) 190–201.
- [26] S.P. Neuman, Theoretical derivation of Darcy's law, *Acta Mechanica* 25 (1977) 153–170.
- [27] R.E. Cunningham, R.J.J. Williams, *Diffusion in Gases and Porous Media*, Plenum Press, New York, 1980.
- [28] G. Iosilevskii, Aerodynamics of permeable membrane wings, *European Journal of Mechanics-B/Fluids* 30 (2011) 534–542.
- [29] P. Saffman, G. Baker, Vortex interactions, *Annual Review in Fluid Mechanics* 11 (1979) 95–122.
- [30] T. Sarpkaya, Computational methods with vortices—the 1988 Freeman scholar lecture, *Journal of Fluids Engineering* 11 (1989) 5–52.
- [31] M.S. Howe, *Theory of Vortex Sound*, Cambridge University Press, Cambridge, 2003.
- [32] A. Manela, On the acoustic radiation of a pitching airfoil, *Physics of Fluids* 25 (2013) 071906.
- [33] S. Mendez, J.D. Eldredge, Acoustic modeling of perforated plates with bias flow for large-eddy simulations, *Journal of Computational Physics* 228 (2009) 4757–4772.
- [34] J.B. Keller, Viscous flow through a grating or lattice of cylinders, *Journal of Fluid Mechanics* 18 (1964) 94–96.
- [35] S. Ergun, Fluid flow through packed columns, *Chemical Engineering Progress* 48 (1952) 89–94.
- [36] A. Dybbs, R.V. Edwards, A new look at porous media fluid mechanics Darcy to turbulent, *Fundamentals of Transport Phenomena in Porous Media* 82 (1984) 199–256.
- [37] C.J. Pennycuik, Predicting wingbeat frequency and wavelength of birds, *Journal of Experimental Biology* 150 (1990) 171–185.